Image Segmentation and Modeling of the Pediatric Tricuspid Valve in Hypoplastic Left Heart Syndrome

Alison M. Pouch[1(✉)], Ahmed H. Aly[2], Andras Lasso[3], Alexander V. Nguyen[4], Adam B. Scanlan[4], Francis X. McGowan[4], Gabor Fichtinger[3], Robert C. Gorman[5], Joseph H. Gorman III[5], Paul A. Yushkevich[1], and Matthew A. Jolley[4]

[1] Department of Radiology, University of Pennsylvania, Philadelphia, PA, USA
pouch@seas.upenn.edu
[2] Department of Bioengineering, University of Pennsylvania, Philadelphia, PA, USA
[3] Laboratory for Percutaneous Surgery, Queen's University, Kingston, Canada
[4] Department of Anesthesiology and Critical Care Medicine,
Children's Hospital of Philadelphia, University of Pennsylvania
Perelman School of Medicine, Philadelphia, PA, USA
[5] Gorman Cardiovascular Research Group, Department of Surgery,
Perelman School of Medicine, University of Pennsylvania, Philadelphia, PA, USA

Abstract. Hypoplastic left heart syndrome (HLHS) is a single-ventricle congenital heart disease that is fatal if left unpalliated. In HLHS patients, the tricuspid valve is the only functioning atrioventricular valve, and its competence is therefore critical. This work demonstrates the first automated strategy for segmentation, modeling, and morphometry of the tricuspid valve in transthoracic 3D echocardiographic (3DE) images of pediatric patients with HLHS. After initial landmark placement, the automated segmentation step uses multi-atlas label fusion and the modeling approach uses deformable modeling with medial axis representation to produce patient-specific models of the tricuspid valve that can be comprehensively and quantitatively assessed. In a group of 16 pediatric patients, valve segmentation and modeling attains an accuracy (mean boundary displacement) of 0.8 ± 0.2 mm relative to manual tracing and shows consistency in annular and leaflet measurements. In the future, such image-based tools have the potential to improve understanding and evaluation of tricuspid valve morphology in HLHS and guide strategies for patient care.

Keywords: Medial axis representation · Multi-atlas segmentation · Tricuspid valve · Hypoplastic left heart syndrome · 3D echocardiography

1 Introduction

Hypoplastic left heart syndrome (HLHS) is a congenital heart disease characterized by underdevelopment of the left heart, including atresia of the mitral and/or aortic valves and an undersized left ventricle that is incapable of supporting systemic circulation. Although the condition constitutes 2–3% of all congenital heart disease [1, 2], HLHS, if left unpalliated, would account for 25–40% of all neonatal cardiac deaths. Palliative surgical intervention is often performed in three stages culminating in the Fontan

M. Pop and G.A. Wright (Eds.): FIMH 2017, LNCS 10263, pp. 95–105, 2017.
DOI: 10.1007/978-3-319-59448-4_10

procedure, which puts systemic and pulmonary circulation in series with a single functioning right ventricle. At all stages, the tricuspid valve is the only functioning atrioventricular valve, and the development of tricuspid regurgitation is understandably associated with morbidity and mortality [3–5]. Accurate assessment of tricuspid valve morphology in HLHS is therefore essential for determining the mechanism of regurgitation and potential techniques for surgical repair [6, 7]. Three-dimensional echocardiography (3DE) captures the complex geometry of the valve in real-time and reduces the subjectivity in image interpretation associated with conventional 2D echocardiography [7–9]. Moreover, 3DE can be used to quantitate morphological abnormalities that may be predictive of clinical outcome in HLHS patients even before the first stage of surgical palliation is performed [5]. Despite a potential relationship between valve morphology and outcome, there is currently no commercial system for semi- or fully automated 3D modeling of tricuspid valves and, in particular, congenitally abnormal valves such as those in HLHS. Although manually cropped volume renderings displayed on the 3DE scanner are valuable for qualitative assessment, they do not automatically generate optimal visualizations or facilitate automatic valve quantification.

Investigation of tricuspid valve morphology in the HLHS population necessitates the development of semi- or fully-automated 3DE image segmentation methods. Valve analysis in this setting, however, presents several challenges relative to valve assessment in the adult population: pediatric patients are more prone to motion than adults, making high resolution EKG gated acquisitions difficult; the images must be acquired transthoracically due to the lack of availability of pediatric transesophageal probes; and there may be visible structural changes in the images introduced by multiple palliative surgeries. To overcome these challenges, we present a strategy that integrates robust image segmentation and shape modeling techniques. Shown in Fig. 1, the tricuspid valve analysis pipeline begins with identification of landmarks that provide initialization for subsequent fully automatic steps. With these landmarks, the input target image is segmented by multi-atlas label fusion (MALF), which uses deformable registration to warp a set of expert-labeled example 3DE images called “atlases” to the target image, and it combines the warped atlas segmentations into a consensus voxel-wise label map of the tricuspid leaflets. Next, in order to make consistent quantitative measurements, a deformable model of the tricuspid valve is warped to capture the geometry of the valve in the label map. The combination of label fusion and deformable modeling has a number of benefits that have been demonstrated in adult mitral and aortic valve applications [10, 11]: it exploits knowledge of tricuspid valve image appearance through the use of expert-labeled atlases; the deformable template has immutable topology, thereby preventing extraneous holes or artifacts in the output model; and the valve is represented volumetrically, as a structure with locally varying thickness. The goal of this work is to demonstrate the first semi-automated image segmentation and geometric modeling of the tricuspid valve in 3DE images from pediatric patients with HLHS. Three-dimensional tricuspid valve models allow interactive 3D visualization and quantitative evaluation of valve morphology, which could improve understanding of tricuspid valve disease in HLHS and potentially translate into enhanced surgical repair.

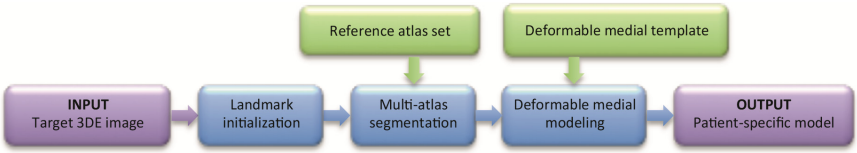

Fig. 1. Tricuspid valve image analysis pipeline.

2 Materials and Methods

2.1 Image Acquisition and Data Sets

Transthoracic 3DE images of the tricuspid valve were acquired from 16 pediatric patients with HLHS aged 4 days to 15 years. Fifteen of these patients had previously undergone the Fontan procedure (stage 3 of surgical palliation). Investigation was approved by the Institutional Review Board at the Children's Hospital of Philadelphia. The images were acquired with the iE33 platform (Philips Medical Systems, Andover, MA) in full volume or 3D zoom mode using an X7 or X5 probe. For each subject, a 3DE image of the closed tricuspid valve in mid-systole (the frame midway between valve opening and closing) was selected for analysis. Systole was chosen since it is the phase of the cardiac cycle during which atrioventricular valves are closed and resist the pressure of ventricular contraction. Abnormal annular shape and leaflet profile during systole has been associated with disease in adult mitral valves [12] and tricuspid valves in HLHS [5, 7]. The images were anonymized and exported in Cartesian format with an approximate resolution of $0.7 \times 0.7 \times 0.5$ mm^3. Each 3DE image was manually traced to create an atlas with the three leaflets (anterior, posterior, and septal) assigned a separate label. In addition, five landmarks were identified in each image for the purpose of initializing multi-atlas segmentation: the mid-septal (MS) annular point, anteroseptal (AS) commissure, the anteroposterior (AP) commissure, the posteroseptal (PS) commissure, and the coaptation point of the three leaflets. Manual tracings of all images were completed by two observers in the "Segments" module of the 3D Slicer application [13]. The proposed segmentation framework was evaluated in a leave-one-out manner: each of the 16 images was segmented using the remaining 15 images and their manual segmentations as atlases for MALF. The resulting segmentations were compared to the manual segmentations to establish the accuracy of the automated method.

2.2 Multi-atlas Segmentation with Joint Label Fusion

With a set of user-identified landmarks, the first step of fully automated tricuspid valve image analysis is multi-atlas joint label fusion. Briefly, a collection of atlases (i.e., 3DE images and labels for the tricuspid leaflets) is registered to a target image, first with a landmark-guided affine transformation and then diffeomorphic deformable registration. The candidate segmentations generated by each atlas are combined to create a consensus label map using the weighted voting method detailed in [14]. Each atlas contributes to the final consensus label map according to locally varying weights determined by

intensity similarities between that atlas and the target image. The voting process also accounts for similarities between atlases to reduce bias attributed to redundancy in the atlas set.

2.3 Deformable Modeling with Medial Axis Representation

MALF generates a label map of the tricuspid valve in the 3DE image, but it does not guarantee the correct topology of the segmentation or provide a straightforward means of computing morphological measurements. To capture the shape of the tricuspid valve in a manner that preserves leaflet topology and enables automated morphometry, deformable modeling with medial axis representation is used to describe valve geometry in the label map generated by label fusion.

Medial axis representation and deformable model fitting. Deformable medial modeling represents an object's geometry in terms of its medial axis, which Blum has defined as a locus of the centers of maximal inscribed balls (MIBs) that lie inside the object and cannot be made any larger without crossing the object boundary [15]. The center of each MIB is associated with a radius R, the distance between that point on the skeleton and the object boundary (Fig. 2). Deformable medial modeling determines the medial axis of a structure through *inverse skeletonization*, wherein the medial axis of the object is first explicitly defined as a continuous parametric manifold $\mathbf{m}:\Omega \rightarrow \mathbb{R}^3, \Omega \in \mathbb{R}^2$ with an associated parametric *thickness* scalar field $R:\Omega \rightarrow \mathbb{R}^+$. The boundary of the object is then derived analytically as described in [16]. Given a label map of an object, a pre-defined template $\{\mathbf{m}, R\}$ is deformed through optimization of a Bayesian objective function with respect to a set of coefficients that parameterize $\mathbf{m}$ and R. The objective function maximizes overlap between the medial template and label image, while enforcing medial constraints and model smoothness through regularization penalties described in [10]. The regularization penalties help to ensure smoothness of the medial edge and prevent leaflet overlap during model deformation. The result is a fitted, patient-specific medial model of the valve. In this work, the tricuspid valve template is a single, non-branching medial manifold (Fig. 2b).

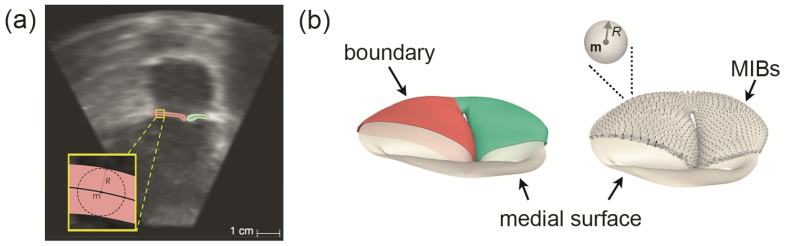

Fig. 2. (a) Image of the tricuspid valve with a 2D medial geometry diagram showing the cross-section of a maximally inscribed ball (MIB) in a leaflet. (b) 3D medial axis diagram of the tricuspid valve showing the medial surface and the cutaway boundary (left) and the MIBs whose centers form the medial surface (right). **m** refers to a point on the medial axis, and R is the radius of the MIB.

Template generation. To obtain a deformable medial template of the tricuspid valve, one of the 16 manual segmentations was selected at random and a triangulated mesh of the segmentation's skeleton was created using the procedure described in [11]. To reduce potential bias associated with a single-subject template, the single-subject template was fitted to all the subject's multi-atlas segmentations, and generalized Procrustes analysis was used to compute a new "average" template. This mean shape, shown in Fig. 2b, served as the final medial template and was deformed to all subjects' MALF results to obtain patient-specific models. While this template generation was not completely unbiased, creation of the mean template served to reduce bias introduced by individual valve geometries.

2.4 Tricuspid Valve Morphometry

To demonstrate automated tricuspid valve morphometry, annular and leaflet measurements were computed from medial models that were deformed to the MALF results and from models that were deformed directly to the manual segmentations:

- Surface area: sum of triangle areas on the atrial side of the anterior, posterior, or septal leaflet
- Bending angle: angle between the normal vectors of the anterior and posterior planes. The anterior plane is defined as the plane that best fits the anterior annular contour and the septal annular contour between the AS commissure and MS point. The posterior plane is defined as the plane that best fits the posterior annular contour and the septal annular contour between the PS commissure and MS point (Fig. 3).

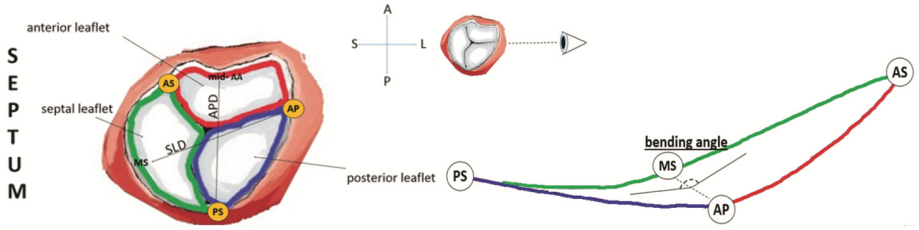

Fig. 3. Schematic of the tricuspid valve (left) and diagram of the annular bending angle measurement as viewed from the AP to MS (right). (A – anterior, P – posterior, S – septal, L – lateral, AP – anteroposterior commissure, AS – anteroseptal commissure, PS – posteroseptal commissure, MS – mid-septum, mid-AA – mid-anterior annulus, SLD – septal-lateral diameter, APD – anteroposterior diameter)

- Annular area: area enclosed by the projection of the annulus onto the annular best-fit plane
- Annular circumference: sum of distances between consecutive points on the annulus
- Septal-lateral diameter (SLD): distance between the MS annular point and the AP commissure, defined as the point on anterior annulus nearest to the posterior annulus

- Antero-posterior diameter (APD): distance between the mid-anterior annular (mid-AA) point and the PS commissure, defined as the point on the posterior annulus nearest to the septal annulus
- Regional annular height: the perpendicular distance from the annulus to the annular best-fit plane, as a function of rotation angle about the annulus
- Global annular height: difference between the maximum and minimum annular height

In addition to annular bending angle, regional annular height was computed as a function of rotation angle around the valve, beginning at the junction of the anterior and septal leaflets. Regional annular height has been shown to be a meaningful descriptor of adult mitral and tricuspid valve geometry [12, 17] and is complementary to annular bending angle in quantifying annular curvature.

3 Results

Examples of manual segmentations, MALF results, and model fittings are shown in Fig. 4 for three pediatric patients with HLHS. The symmetric mean boundary error (MBE) between the manual segmentations and the deformable medial model fitted to the multi-atlas segmentation results was 0.8 ± 0.2 mm. For reference, the MBE between the manual segmentations and the deformable models fitted directly to the manual segmentations was 0.3 ± 0.1 mm, and the MBE between the manual and multi-atlas segmentations without model fitting was 0.7 ± 0.2 mm. Table 1 lists and compares morphological measurements derived from medial models fitted to the multi-atlas segmentation results and directly to the manual segmentations. Results of a paired Student's *t*-test and the intraclass correlation coefficient (ICC) are given.

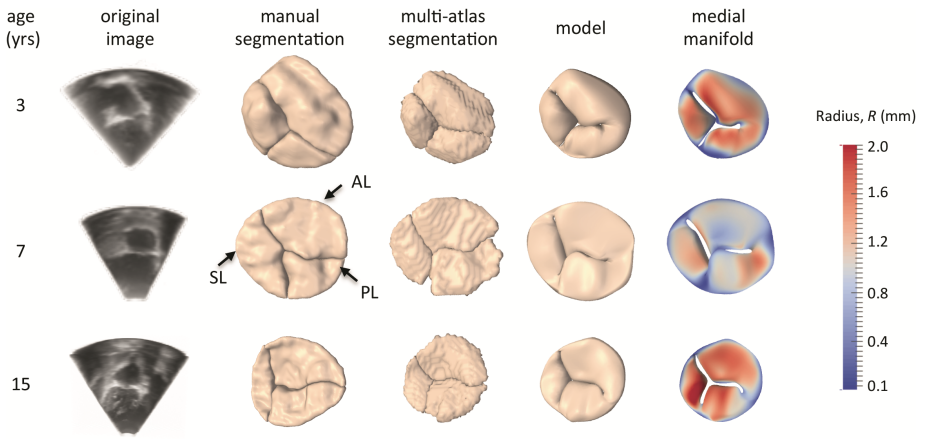

Fig. 4. Tricuspid valve segmentation results for three patients. The medial surface is shown with the radius function in color (rightmost column).

Table 1. Measurements derived from the deformable models fitted to the multi-atlas (automated) and manual segmentations. The p-value, bias, and intraclass correlation (ICC) relate to the comparison of automated and manual measurements, and r_{BSA} is the Pearson correlation between the percent error in the automated measurement and the patient's BSA.

Measurement	Automated segmentation	Manual segmentation	p-value	Bias	ICC	r_{BSA}
Atrial anterior leaflet surface area (mm^2)	407.6 ± 129.2	436.5 ± 159.6	0.577	−28.9	0.75	−0.27
Atrial posterior leaflet surface area (mm^2)	259.8 ± 102.1	325.7 ± 155.5	0.167	−65.9	0.67	−0.12
Atrial septal leaflet surface area (mm^2)	210.0 ± 88.3	290.5 ± 114.0	0.033	−80.5	0.52	−0.17
Bending angle (degrees)	165.3 ± 10.4	168.1 ± 8.13	0.401	−2.8	0.78	−0.05
Annular area (mm^2)	716.2 ± 245.6	819.1 ± 294.1	0.292	−102.8	0.84	0.00
Annular circumference (mm)	96.4 ± 17.1	102.4 ± 19.9	0.369	−6.0	0.86	−0.08
Septal-lateral diameter (mm)	30.2 ± 5.7	32.3 ± 7.1	0.359	−2.1	0.89	−0.43
Anterior-posterior diameter (mm)	29.5 ± 5.8	30.8 ± 6.6	0.567	−1.3	0.88	−0.06
Global annular height (mm)	3.7 ± 1.5	3.4 ± 1.3	0.613	0.3	0.69	−0.12

To assess segmentation and measurement accuracy relative to valve size, MBE and percent error in the measurements in Table 1 were evaluated in terms of body surface area (BSA), which has a known relationship with valve size: valve diameter scales linearly with $\mathrm{BSA}^{1/2}$ and valve area scales linearly with BSA [18]. In Fig. 5, MBE is plotted as a function of $\mathrm{BSA}^{1/2}$, showing no significant linear relationship (Pearson correlation $r = 0.21$, $p = 0.4$). The percent error in linear measurements such as antero-lateral diameter was evaluated as a function of $\mathrm{BSA}^{1/2}$, and the percent error in area measurements such as leaflet surface area was evaluated as a function of BSA. No statistically significant linear relationship between measurement accuracy and $\mathrm{BSA}^{1/2}$ or BSA was observed (Table 1, Pearson correlation $|r| < 0.43$, $p > 0.1$).

In Fig. 6, regional annular height is plotted as a function of rotational angle about the annulus. Here, regional annular height is shown for each individual subject (black curves), and the mean regional annular height for the population is shown in red.

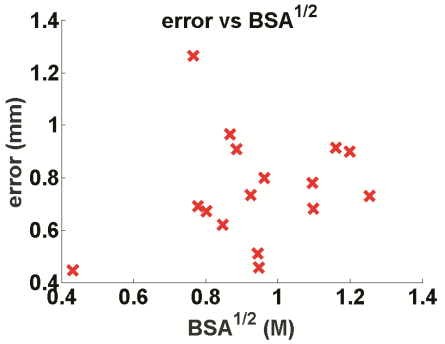

Fig. 5. Mean boundary error as a function of the square root of body surface area (BSA).

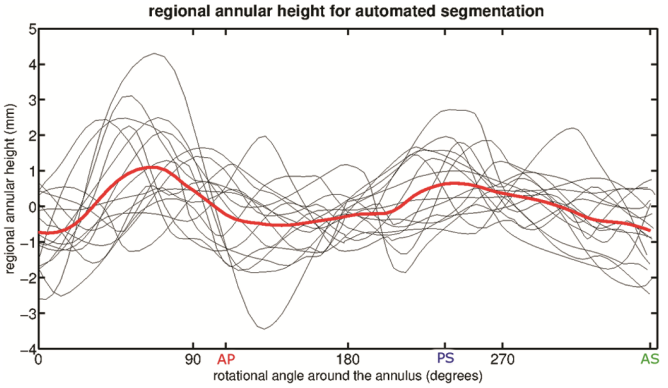

Fig. 6. Annular height as a function of rotation angle around the annulus. Black curves correspond to individual patients, and red is the mean regional height. (AP – anteroposterior commissure, PS – posteroseptal commissure, AS – anteroseptal commissure at 0°) (Color figure online)

4 Discussion

The basic three-dimensional structure of the tricuspid valve in HLHS has been shown to be associated with valve competence and with patient survival [5, 7]. The ability to rapidly, automatically, and comprehensively characterize tricuspid valve morphology from readily available transthoracic 3DE is critical to further understanding of valve dysfunction and translation to clinical application. This study is the first to demonstrate a semi-automated method for image segmentation, geometric modeling, and morphometry of the tricuspid valve in patients with HLHS. Further, this work demonstrates preliminary evidence that the adaptation and evolution of image processing algorithms that have effectively modeled mitral valves in transesophageal 3DE in the adult population are applicable to transthoracic images in congenital heart disease.

Accuracy of automatic segmentation and quantification is essential to reliable valve modeling. MBE between the manual segmentation and the medial models fitted to the results of multi-atlas segmentation (0.8 ± 0.2 mm) was on the order of 1–2 voxels. The advantage of a medial representation over multi-atlas segmentation alone is that deformable modeling enables consistent morphometry in a patient population. Medial axis representation, in particular, distinguishes the atrial and ventricular surfaces of the leaflets and facilitates measurements such as locally varying thickness (derived from the parameter R). The manual versus semi-automatic segmentation comparison in this study is on par with studies of mitral and aortic valve segmentation in adult transesophageal 3DE images, wherein MBEs of 1.54 ± 1.17 mm [19], 0.59 ± 0.49 mm [20], and 0.6 ± 0.2 mm [10] have been reported. In this study, no linear relationship was observed between segmentation accuracy and $BSA^{1/2}$ (Fig. 5), suggesting that the segmentation algorithm is applicable to tricuspid valves of a wide size range (53–128 mm in circumference) in the HLHS population. Since the majority of the subjects in this study had a BSA lower than 0.6 M^2, a larger cohort of patients ranging from neonates to adults will need to be assessed in the future to evaluate broad applicability.

In addition to image segmentation, this work demonstrates an evolving tool for evaluation of tricuspid valve morphology in HLHS (Table 1, Figs. 5 and 6). When comparing measurements derived from deformable models fitted to the manual and multi-atlas segmentations, no significant difference ($p < 0.05$) was observed except for measurement of septal leaflet surface area. Except for this measurement, the intraclass correlations between manual and automatically derived measurements were good to excellent (Table 1). Illustrating individual and mean regional annular height, Fig. 6 demonstrates the ability to characterize localized tricuspid annular geometry from medial models. When compared to normal adult mitral annuli, which have an average height of 7 ± 2 mm and are characterized by a distinctive saddle shape [12], both the individual and average regional annular height contours of the HLHS patients in Fig. 6 suggest that the tricuspid annulus is relatively flat at mid-systole, but exhibits substantial variability between patients. As a measure of annular flatness, bending angle in prestage 1 palliation has been associated with tricuspid valve failure at medium-term follow-up of HLHS [5]. The bending angles computed in this study (Table 1) are comparable to those reported in the literature for HLHS patients [7].

While this study is a proof of concept of segmentation and modeling of the tricuspid valve in pediatric transthoracic 3DE, future work will focus on expanding atlases and application across a large age range, making these tools fully automated, and extending the current leaflet quantification metrics. Segmentation at multiple frames in the cardiac cycle, as well as evaluation of intra- and inter-observer variability in automated valve analysis, are important extensions of this work. Future application of this evolving methodology to larger HLHS populations may facilitate valvular shape characterization, associate morphological metrics with clinical outcomes, and eventually translate into clinical decision making.

Acknowledgement. This work was supported by grant numbers EB017255 and HL103723 from the National Institutes of Health, as well as the Children's of Hospital of Philadelphia Department of Anesthesia and Critical Care Medicine, Cancer Care Ontario with funds provided by the Ontario Ministry of Health and Long-Term Care, the Natural Sciences and Engineering Research Council of Canada (NSERC), and the Neuroimage Analysis Center supported by the National Institute of Biomedical Imaging and Bioengineering (P41 EB015902).

References

1. Gordon, B.M., Rodriguez, S., Lee, M., Chang, R.K.: Decreasing number of deaths of infants with hypoplastic left heart syndrome. J. Pediatr. **153**(3), 354 (2008)
2. Reller, M.D., Strickland, M.J., Riehle-Colarusso, T., Mahle, W.T., Correa, A.: Prevalence of congenital heart defects in metropolitan Atlanta, 1998–2005. J. Pediatr. **153**(6), 807 (2008)
3. Barber, G., Helton, J.G., Aglira, B.A., Chin, A.J., Murphy, J.D., Pigott, J.D., Norwood, W.I.: The significance of tricuspid regurgitation in hypoplastic left-heart syndrome. Am. Heart J. **116**, 1563–1567 (1988)
4. Elmi, M., Hickey, E.J., Williams, W.G., Van Arsdell, G., Caldarone, C.A., McCrindle, B.W.: Long-term tricuspid valve function after Norwood operation. J. Thorac. Cardiovasc. Surg. **142**, 1341–1347 (2011). e4
5. Kutty, S., Colen, T., Thompson, R.B., Tham, E., Li, L., Vijarnsorn, C., Polak, A., Truong, D.T., Danford, D.A., Smallhorn, J.F., Khoo, N.S.: Tricuspid regurgitation in hypoplastic left heart syndrome. Circ. Cardiovasc. Imaging **7**, 765–772 (2014)
6. Bharucha, T., Honjo, O., Seller, N., Atlin, C., Redington, A., Caldarone, C.A., van Arsdell, G., Mertens, L.: Mechanisms of tricuspid valve regurgitation in hypoplastic left heart syndrome: a case-matched echocardiographic-surgical comparison study. Eur. Heart J. Cardiovasc. Imaging **14**, 135–141 (2013)
7. Takahashi, K., Mackie, A.S., Rebeyka, I.M., Ross, D.B., Robertson, M., Dyck, J.D., Inage, A., Smallhorn, J.F.: Two-dimensional versus transthoracic real-time three-dimensional echocardiography in the evaluation of the mechanisms and sites of atrioventricular valve regurgitation in a congenital heart disease population. J. Am. Soc. Echocardiogr. **23**, 726–734 (2010)
8. Badano, L.P., Agricola, E., Perez de Isla, L., Gianfagna, P., Zamorano, J.L.: Evaluation of the tricuspid valve morphology and function by transthoracic real-time three-dimensional echocardiography. Eur. J. Echocardiogr. **10**, 477–484 (2009)
9. Anwar, A.M., Geleijnse, M.L., Soliman, O.I., McGhie, J.S., Frowijn, R., Nemes, A., van den Bosch, A.E., Galema, T.W., Ten Cate, F.J.: Assessment of normal tricuspid valve anatomy in adults by real-time three-dimensional echocardiography. Int. J. Cardiovasc. Imaging **23**, 717–724 (2007)
10. Pouch, A.M., Wang, H., Takabe, M., Jackson, B.M., Gorman 3rd, J.H., Gorman, R.C., Yushkevich, P.A., Sehgal, C.M.: Fully automatic segmentation of the mitral leaflets in 3D transesophageal echocardiographic images using multi-atlas joint label fusion and deformable medial modeling. Med. Image Anal. **18**, 118–129 (2014)
11. Pouch, A.M., Tian, S., Takebe, M., Yuan, J., Gorman, R., Cheung, A.T., Wang, H., Jackson, B.M., Gorman, J.H., Gorman, R.C., Yushkevich, P.A.: Medially constrained deformable modeling for segmentation of branching medial structures: application to aortic valve segmentation and morphometry. Med. Image Anal. **26**, 217–231 (2015)

12. Jassar, A.S., Vergnat, M., Jackson, B.M., McGarvey, J., Cheung, A.T., Ferrari, G., Woo, Y.J., Acker, M.A., Gorman, R.C., Gorman III, J.H.: Regional annular geometry in patients with mitral regurgitation: Implications for annuloplasty ring selection. Ann. Thorac. Surg. **97**(1), 64–70 (2014)
13. Fedorov, A., Beichel, R., Kalpathy-Cramer, J., Finet, J., Fillion-Robin, J.-C., Pujol, S., Bauer, C., Jennings, D., Fennessy, F.M., Sonka, M., Buatti, J., Aylward, S.R., Miller, J.V., Pieper, S., Kikinis, R.: 3D slicer as an image computing platform for the quantitative imaging network. Magn. Reson. Imaging **30**(9), 1323–1341 (2012)
14. Wang, H., Suh, J.W., Das, S., Pluta, J., Craige, C., Yushkevich, P.: Multi-atlas segmentation with joint label fusion. IEEE Trans. Pattern Anal. Mach. Intell. **35**(3), 611–623 (2013)
15. Blum, H.: A transformation for extracting new descriptors of shape. In: Wathen-Dunn, W. (ed.) Models for the Perception of Speech and Visual Form, pp. 362–380. MIT Press, Cambridge (1967)
16. Yushkevich, P.A., Zhang, H., Gee, J.C.: Continuous medial representation for anatomical structures. IEEE Trans. Med. Imaging **25**(12), 1547–1564 (2006)
17. Fukuda, S., Saracino, G., Matsumura, Y., Daimon, M., Tran, H., Greenberg, N.L., Hozumi, T., Yoshikawa, J., Thomas, J.D., Shiota, T.: Three-dimensional geometry of the tricuspid annulus in healthy subjects and in patients with functional tricuspid regurgitation. Circulation **114**(suppl I), I-492–I-498 (2006)
18. Sluysmans, T., Colan, D.: Theoretical and empirical derivation of cardiovascular allometric relationships in children. J. Appl. Physiol. **99**, 445–457 (2005)
19. Ionasec, R.I., Voigt, I., Georgescu, B., Wang, Y., Houle, H., Vega-Higuera, F., Navab, N., Comaniciu, D.: Patient-specific modeling and quantification of the aortic and mitral valves from 4-D cardiac CT and TEE. IEEE Trans. Med. Imaging **29**, 1636–1651 (2010)
20. Schneider, R.J., Tenenholtz, N.A., Perrin, D.P., Marx, G.R., del Nido, P.J., Howe, R.D.: Patient-specific mitral leaflet segmentation from 4D ultrasound. Med. Image Comput. Comput. Assist. Interv. **14**, 520–527 (2011)